Journal of Materials Chemistry B

ROYAL SOCIETY OF CHEMISTRY

PAPER

View Article Online
View Journal

Cite this: DOI: 10.1039/d5tb02893k

Evaluation of Fe-MOF/graphene nanocomposites for non-enzymatic electrochemical sensing of acetaminophen

Jithin Rafi, [a] Thangavelu Kokulnathan, [b] Tzyy-Jiann Wang, *[b] Murugan Velmurugan[c] and Bernaurdshaw Neppolian*[a]

Distribution and accumulation of pharmaceuticals in the environment are of growing concern due to their persistence and potential adverse effects on human health and aquatic ecosystems. In this study, we present a straightforward synthesis strategy to fabricate an electrocatalytic nanocomposite with the iron–metal–organic framework supported on graphene sheets (Fe-MOF/GR) for non-enzymatic electrochemical detection of acetaminophen (APAP). The material characteristics of the Fe-MOF/GR nanocomposite were comprehensively analyzed using various microscopic and spectroscopic techniques. The Fe-MOF/GR-modified electrode demonstrates a 3.97-fold increase in the peak oxidation current compared to the bare electrode for APAP detection. The excellent electrocatalytic activity of the Fe-MOF/GR-based electrochemical sensor toward APAP detection can be attributed to the synergistic effects of numerous exposed electro-active sites, high electrocatalytic activity, and exceptional conductivity. Under optimal synthesis conditions, the proposed electrochemical sensor exhibits a low detection limit of 10 nM, a high sensitivity of 6.7 μM^{-1} cm^{-2}, and a broad linear range of 0.05 to 105.6 μM. Besides, it showcases high selectivity (<7%), satisfactory repeatability (1.6%), and robust reproducibility (2.02%). Its practical feasibility is demonstrated through its successful application in quantifying APAP in real biological and environmental water samples, yielding satisfactory recovery values. The findings of this study suggest that the proposed electrochemical sensor is a promising candidate for practical applications in APAP detection.

Received 24th December 2025,
Accepted 29th April 2026

DOI: 10.1039/d5tb02893k

rsc.li/materials-b

1. Introduction

Pharmaceuticals have significantly advanced the medical treatment system and are crucial to global healthcare.[1] However, the increase in their production and consumption has led to their accumulation in environmental resources and raises urgent concerns about pharmaceutical pollution in water sources. Acetaminophen (APAP, *N*-acetyl-*p*-aminophenol, or paracetamol) is one of the most widely used antipyretic analgesics and is often found in water at concentrations exceeding hundreds of ppb.[2] Elevated APAP concentrations can cause liver damage and neurotoxic issues in humans, and harm aquatic and animal life.[3] Its hepatotoxicity is a leading cause of acute liver failure in the United States and other Western nations.[4] Therefore, the development of cost-effective, sensitive, and user-friendly approaches for APAP determination is essential for medical monitoring of biological fluids and effective environmental management.

There are many analytical methods for the detection of APAP, including high-performance liquid chromatography,[5] liquid chromatography-tandem mass spectroscopy,[6] colorimetry,[7] fluorescence spectrophotometry,[8] flow injection chemiluminescence,[9] and electrophoresis.[10] However, these methods often suffer from slow response time, high cost, and complex instrumentation, which highlights the need for developing more efficient detection methods. In contrast, the electrochemical method offers attractive advantages, such as rapid response, portable instrumentation, low cost, and easy fabrication, which make it suitable for real-time detection.[11–14] There are many reports on the electrochemical detection of APAP with the focus on developing various electrocatalysts as electrode materials.[15–18] Therefore, it is crucial to explore electrocatalysts for electrochemical sensors that can accurately and effectively detect APAP.

Two-dimensional (2D) materials have garnered significant interest as electrode materials for electrochemical applications. Metal–organic frameworks (MOFs), a class of layered 2D

[a] *Energy and Environmental Remediation Lab, Department of Chemistry, Faculty of Engineering and Technology, SRM Institute of Science and Technology, Kattankulathur, Chengalpattu 603203, Tamil Nadu, India. E-mail: neppolib@srmist.edu.in*
[b] *Department of Electro-Optical Engineering, National Taipei University of Technology, Taipei 10608, Taiwan. E-mail: f10939@ntut.edu.tw*
[c] *Department of Chemistry, K. Ramakrishnan College of Technology, Samayapuram, Tiruchirappalli 621112, Tamil Nadu, India*

materials, have attracted considerable attention due to their wide range of catalytic applications.[19–22] Their widespread capabilities stem from their tunable pore structure, large surface area, facile synthesis, and ease of functionalization. Adsorptive and π–π interactions have been effectively utilized for the extraction of APAP from biological fluids.[23–25] Iron-based MOFs (Fe-MOFs) exhibit versatile properties, including high structural stability, ease of synthesis, and the presence of sufficient unsaturated metal coordination sites.[26] The amino-functionalized Fe-MOF known as 'Material Institute of Lavoisier-101' (NH_2-MIL-101(Fe)) demonstrates various catalytic properties suitable for electrochemical applications.[27,28] Despite the limited conductivity of pure MOFs, they can be transformed into composites with carbonaceous nanomaterials for enhancing their properties while retaining their inherent advantages.[29,30]

Among various carbonaceous nanomaterials, graphene (GR) has a hexagonal lattice composed of carbon atoms with one-atom thickness by constituting a 2D sp^2-hybridized carbon allotrope.[31] Its delocalized π–π electron configuration can efficiently enhance electron transport while its 2D nanotexture provides great surface area and high structural order, which make it an optimal platform with high electrocatalytic activity. Furthermore, the combination of GR nanomaterials with various functionalities and the diverse array of Fe-MOF structures and morphologies opens up promising and exciting possibilities. Their synergies could create a wide range of nanocomposites with an increased number of electroactive sites. Therefore, the composites combining Fe-MOF and GR would be promising for the effective electrochemical detection of APAP. However, this combination has not been explored previously.

Building on these insights, we propose the combination of Fe-MOF and GR as an efficient electrocatalyst for the electrochemical detection of APAP. Various analytical methods were employed to analyze and characterize the crystal structure, the elemental composition, and the surface morphology of the Fe-MOF/GR nanocomposite. Cyclic voltammetry (CV) analysis reveals that the Fe-MOF/GR-modified disposable electrode exhibits significantly enhanced electrocatalytic activity for detecting APAP compared to other modified electrodes. The use of differential pulse voltammetry (DPV) analysis can effectively detect APAP to achieve low limits of detection (LOD), high sensitivity, and a wide linear detection range. The proposed electrochemical detection platform demonstrates excellent anti-interference effect, repeatability, and reproducibility in detecting APAP. Moreover, the prepared Fe-MOF/GR detection platform was successfully utilized for the electrochemical determination of APAP in actual samples. Our work highlights the potential of the Fe-MOF/GR nanocomposite in the sensing technology and opens new avenues for future research and development in the electrochemical field.

2. Experimental section

The chemicals and instrumental techniques are included in the supplementary information.

2.1 Synthesis of the Fe-MOF

The Fe-MOF was synthesized by the hydrothermal method with slight modifications.[32] Typically, 0.405 g of $FeCl_3$ and 0.362 g of NH_2-BDC were dissolved in 30 mL of DMF under stirring for 2 h. The precursor solution was transferred to a stainless-steel autoclave and then was maintained in an oven at 120 °C for 20 h. The resulting reddish-brown powder was then washed three times with fresh DMF and dried at 70 °C for 24 h.

2.2 Preparation of Fe-MOF/GR nanocomposites

The Fe-MOF and the GR were incorporated using the wet impregnation method at room temperature. Pure GR was distributed in 1 mL of DMF under ultrasonication for 1 h to facilitate the exfoliation of GR sheets. The synthesized Fe-MOF was mixed into this solution and stirred for 2 h. The dispersions of Fe-MOF/GR nanocomposites with the ratios of 1 : 1, 1 : 2, 1 : 3, 2 : 1, and 3 : 1 were prepared and then washed with ethanol by centrifugation to remove any unattached material. The final product was dried at 60 °C for 12 hr.

2.3 Electrode fabrication

The working electrode was polished using 0.05 μm alumina powder. After polishing, the GCE underwent ultrasonic treatment to remove any remaining alumina powder from its surface. A 5 μL drop of the Fe-MOF/GR nanocomposite dispersion was deposited onto the pre-cleaned GCE and dried in an oven at 40 °C. For comparison, the same amount of Fe-MOF and GR was separately drop-cast onto the GCE surface.

3. Results and discussion

3.1 Structural and morphological characterization

The structural analysis of Fe-MOF, GR, and the Fe-MOF/GR nanocomposite was conducted using XRD, as shown in Fig. 1A. The diffraction peaks of the Fe-MOF at the 2θ values of 9.3°, 10.4°, 16.6°, 18.7°, 20.9°, 25.3°, and 29.7° are consistent with the simulated patterns of the MIL group (CCDC No. 605510) and align well with the reported XRD patterns of NH_2-MIL-101(Fe) in the literature.[33] The GR exhibits a sharp peak at 26.5° corresponding to the (0 0 2) crystalline plane of typical graphene sheets (ICDD No. 75-2078).[34] The Fe-MOF/GR nanocomposite reveals all the characteristic XRD peaks of Fe-MOF and GR. Notably, the XRD peaks were slightly shifted to lower 2θ values, which indicates the lattice expansion and confirms the successful formation of the Fe-MOF/GR nanocomposite.

The FTIR spectra of Fe-MOF, GR, and the Fe-MOF/GR nanocomposite are presented in Fig. 1B. The Fe-MOF exhibits characteristic bands at 1587 cm^{-1} and 1380 cm^{-1}, which correspond to the asymmetric C=O and C–O stretching vibrations of carboxylate groups. The metal-oxygen (Fe–O) stretching vibration is observed in the range of 580 to 440 cm^{-1}. Additionally, the N–H stretching vibration of the primary amine in the ligand appears as a doublet around 3300 cm^{-1} while the C–N stretching vibration is noted near 1250 cm^{-1}.[35] In contrast, GR exhibits limited bands due to its composition of solely

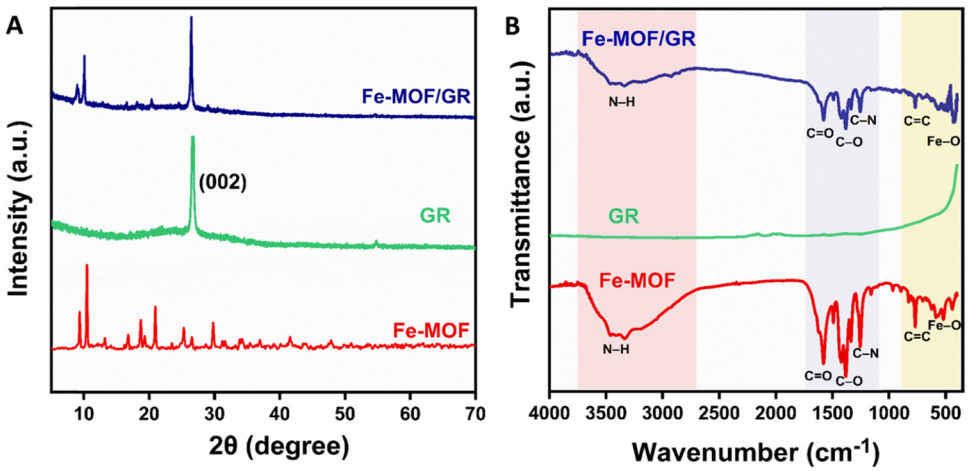

Fig. 1 (A) XRD patterns and (B) FTIR spectra of Fe-MOF, GR and the Fe-MOF/GR nanocomposite.

sp^2-hybridized carbon atoms arranged in a highly symmetric hexagonal lattice, which lacks polar functional groups. The Fe-MOF/GR nanocomposite shows the FTIR bands corresponding to all characteristic bands of Fe-MOF and GR. However, the N–H band becomes less broad and the intensities of the FTIR bands decrease. The FTIR results provide further evidence for the successful formation of the Fe-MOF/GR nanocomposite.

Raman spectroscopy is a crucial non-destructive method for evaluating the structural integrity and quality of carbon-based materials. In the Raman spectrum of GR in Fig. S1, three prominent Raman peaks are observed at 1342 cm^{-1}, 1567 cm^{-1}, and 2677 cm^{-1}, which correspond to the D, G, and 2D bands, respectively. The D band corresponds to the structural disorders or defects, which are primarily associated with the sp^3 hybridized carbon atoms at the edges of graphene. The G band arises from the first-order scattering of the E_{2g} vibrational mode in the sp^2 hybridized carbon networks, while the 2D band results from a two-phonon double resonance process.[36] Notably, the intensity ratio of the D band to the G band (I_D/I_G) increases after the formation of the composite, which suggests a higher degree of defects in the material. This observation confirms the formation of van der Waals interactions between Fe-MOF and GR and highlights the enhanced structural complexity of the nanocomposite.

The electrostatic interaction in the Fe-MOF/GR nanocomposite can be elucidated by conducting the zeta potential analysis. In Fig. S2, the zeta potential of the Fe-MOF exhibits a slight positive charge of +4.3 mV while that of GR displays a negative zeta potential of −55.0 mV. In the 1 : 1 Fe-MOF/GR nanocomposite, the zeta potential remains negative, which is significant for the electrostatic interaction with the positively charged APAP analyte molecules on the electrode surface.

XPS analysis was employed to investigate the electronic structure and the elemental composition of the Fe-MOF/GR nanocomposite. The XPS survey spectrum in Fig. S3 displays the presence of iron (Fe), carbon (C), nitrogen (N), and oxygen (O) elements within the Fe-MOF/GR nanocomposite. In the high-resolution Fe 2p spectrum of Fig. 2A, two prominent peaks at 725.4 eV and 711.7 eV correspond to Fe $2p_{1/2}$ and Fe $2p_{3/2}$. Further deconvolution of the spectrum reveals additional peaks at 728.2 eV, 725.4 eV, 712.4 eV, and 711.2 eV, which are characteristic of Fe(III) species. A satellite peak at 717.4 eV, typical for Fe(III), confirms that the iron in the Fe-MOF predominantly exists in the +3-oxidation state.[35] The C 1s spectrum in Fig. 2B displays three distinct peaks at binding energies of 284.4 eV, 285.4 eV, and 288.4 eV, which correspond to the C–C/C═C, C–N, and C═O bonds, respectively. In the O 1s spectrum of Fig. 2C, three deconvoluted peaks at 529.9 eV, 531.6 eV, and 532.9 eV are associated with the Fe–O, C═O, and C–O bonds. The N 1s spectrum in Fig. 2D reveals two peaks at 398.8 eV and 399.9 eV, which correspond to the C–NH_2 bonding and the presence of ammonium cations.[37] The XPS results confirm the successful synthesis of the Fe-MOF/GR nanocomposite.

The surface morphology of Fe-MOF, GR, and the Fe-MOF/GR nanocomposite was analyzed using FESEM (Fig. 3) and TEM (Fig. S4). As shown in Fig. 3(A) and (B) and Fig. S4A, the Fe-MOF exhibits a bipyramidal hexagonal spindle-like structure with well-defined edges. The FESEM images of GR in Fig. 3(C) and (D) reveal an ultrathin nanosheet-like morphology. For the Fe-MOF/GR nanocomposite, the FESEM images in Fig. 3(E) and (F) and the TEM images in Fig. S4(B) and (C) demonstrate that the spindle-like hexagonal prisms of Fe-MOF are uniformly arranged over the GR nanosheets, likely facilitated by π–π interactions between the two components. The HRTEM image in Fig. S4D provides further structural insights. Clear lattice fringes with *d*-spacings of 0.35 nm and 0.093 nm were observed, corresponding to the high-order crystallographic planes of the cubic Fe-MOF and the GR support. The corresponding SAED pattern in Fig. S4E displays a series of well-defined concentric polycrystalline diffraction rings embedded with bright spots. These concentric rings correspond to the polycrystalline cubic phase of MIL-101(Fe), while the bright diffraction spots indicate high crystallinity and successful hybrid formation with the GR network. Fig. S5A presents the combined EDX image of the Fe-MOF/GR nanocomposite, and the corresponding EDX

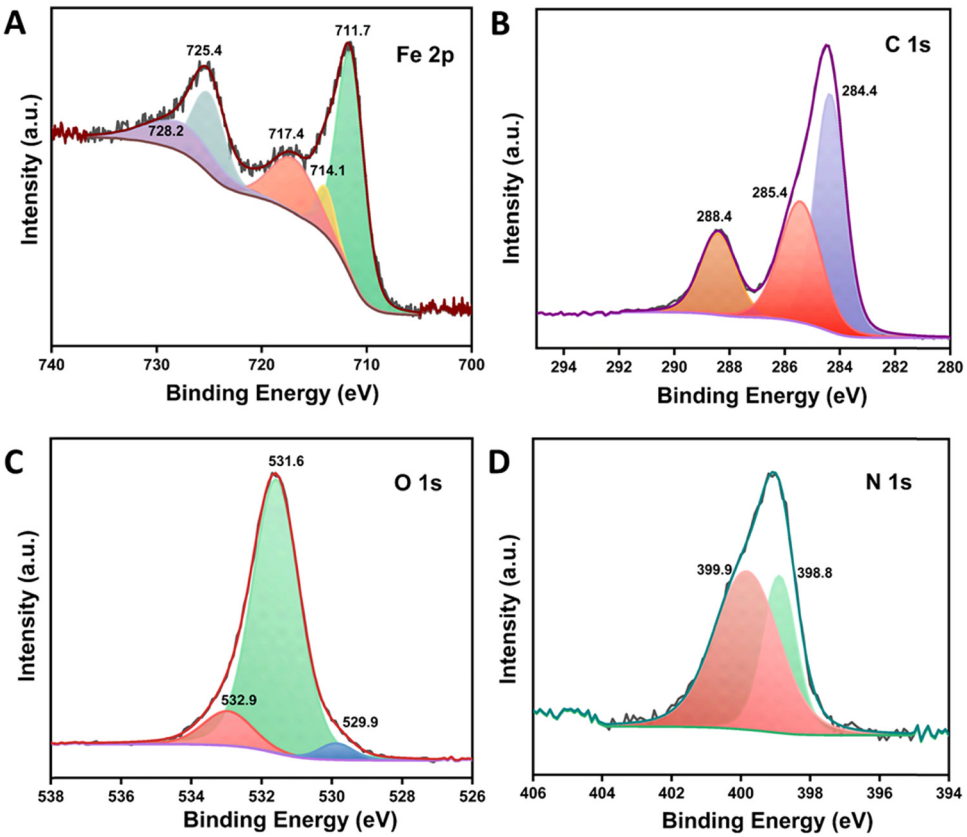

Fig. 2 High-resolution XPS spectra of the Fe-MOF/GR nanocomposite for (A) Fe 2p, (B) C 1s (C) N 1s and (D) O 1s elements.

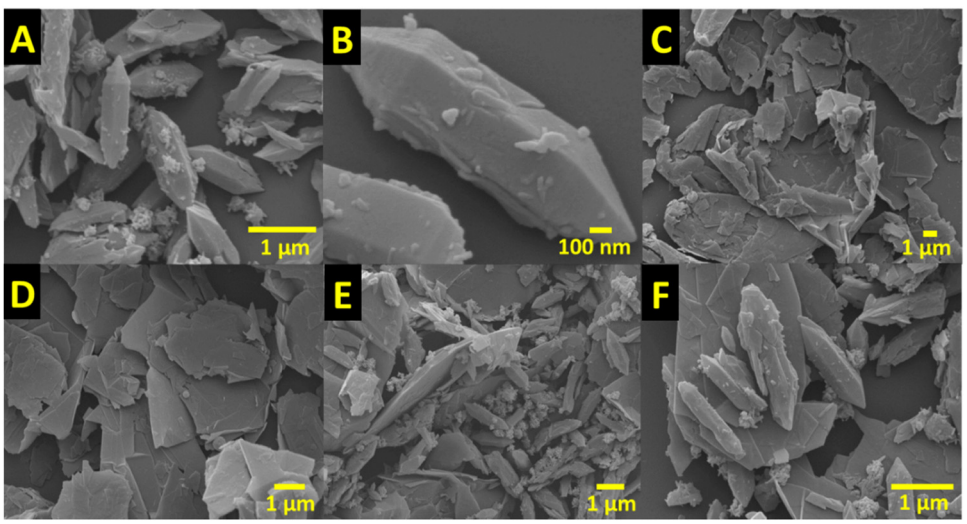

Fig. 3 FESEM images of (A), (B) Fe-MOF, (C), (D) GR and (E), (F) the Fe-MOF/GR nanocomposite.

spectrum in Fig. S5B confirms the presence of Fe, C, N, and O elements. The elemental mapping images in Fig. S5(C)–(F) illustrate the uniform distribution of these elements throughout the nanocomposite. Collectively, these characterizations confirm the successful synthesis of the Fe-MOF/GR nanocomposite.

BET nitrogen adsorption–desorption measurement was performed to evaluate the textural properties of the materials (Fig. S6). The Fe-MOF exhibits a specific surface area of 26.188 $m^2 g^{-1}$, while the Fe-MOF/GR nanocomposite shows a slightly higher surface area of 28.502 $m^2 g^{-1}$. Both samples display adsorption–desorption characteristics of type-IV behavior, indicating the presence of mesoporous structures. The observed enhancement in surface area for the Fe-MOF/GR nanocomposite is attributed to the incorporation of graphene

sheets, which reduce particle agglomeration and help preserve accessible porosity within the composite framework.

3.2 Electrochemical characterization

Electrochemical impedance spectroscopy (EIS) was employed to study the electron transport characteristics of the bare GCE, Fe-MOF/GCE, GR/GCE, and Fe-MOF/GR/GCE with the results shown in Fig. 4A. The Randles equivalent circuit model in the inset of Fig. 4A includes the solution resistance (R_s), the double layer capacitance (C_{dl}), the charge transfer resistance (R_{ct}), and the Warburg impedance (W). The semicircle in the high-frequency region of the EIS curve reflects the R_{ct} value of the electrode. The R_{ct} values are 156.9 Ω for the bare GCE, 62.57 Ω for the Fe-MOF/GCE, 16.49 Ω for the GR/GCE, and 12.13 Ω for the Fe-MOF/GR/GCE. The distribution of R_{ct} values in Fig. 4B indicates that the Fe-MOF/GR/GCE exhibits the lowest R_{ct} value compared to other electrodes, which indicates its significantly enhanced electrochemical performance.

The electrochemical active surface area (EASA) of the bare GCE, Fe-MOF/GCE, GR/GCE, and Fe-MOF/GR/GCE was measured using the CV method with the solution containing 5 mM $[Fe(CN)_6]^{3-/4-}$ and 0.1 M KCl at various scan rates. For all the CV curves in Fig. S7–S10, the peak redox current progressively increases with the scan rate from 10 to 100 mV s^{-1}. In the insets of Fig. S7–S10, the observed linear relation between the peak current and the square root of the scan rate indicates the diffusion-controlled behavior in the electrochemical reaction. The EASA was calculated using the Randle–Sevick equation.[38]

$$I_p = 2.69 \times 10^5 A D^{1/2} n^{3/2} \upsilon^{1/2} C,$$

where I_p is the peak redox current, A is the surface area of the electrode, D is the diffusional coefficient, n is the number of electrons, υ is the scan rate, and C is the analyte concentration. The calculated EASA values for the bare GCE, the Fe-MOF/GCE, the GR/GCE, and the Fe-MOF/GR/GCE are 0.049, 0.114, 0.136, and 0.155 cm^2, respectively. The largest EASA value of the fabricated Fe-MOF/GR/GCE confirms its enhanced electrochemical performance.

3.3 Electrochemical analysis of APAP

The electrocatalytic behavior of the bare GCE, Fe-MOF/GCE, GR/GCE, and Fe-MOF/GR/GCE was examined using the CV method in 0.05 M PBS with 150 μM APAP at the scan rate of 50 mV s^{-1}, as shown in Fig. 4C. The bare GCE shows the peak oxidation at 0.57 V while the Fe-MOF/GCE shows that at 0.52 V, which indicates the enhancement of the reaction dynamics. For the GR/GCE, the reversible redox reaction occurs at 0.44 V, which benefits from GR's high conductivity and high electroactive surface area. The Fe-MOF/GR/GCE further improves the electrocatalytic activity of APAP with the oxidation occurring at 0.43 V and reduction occurring at 0.41 V, which correspond to

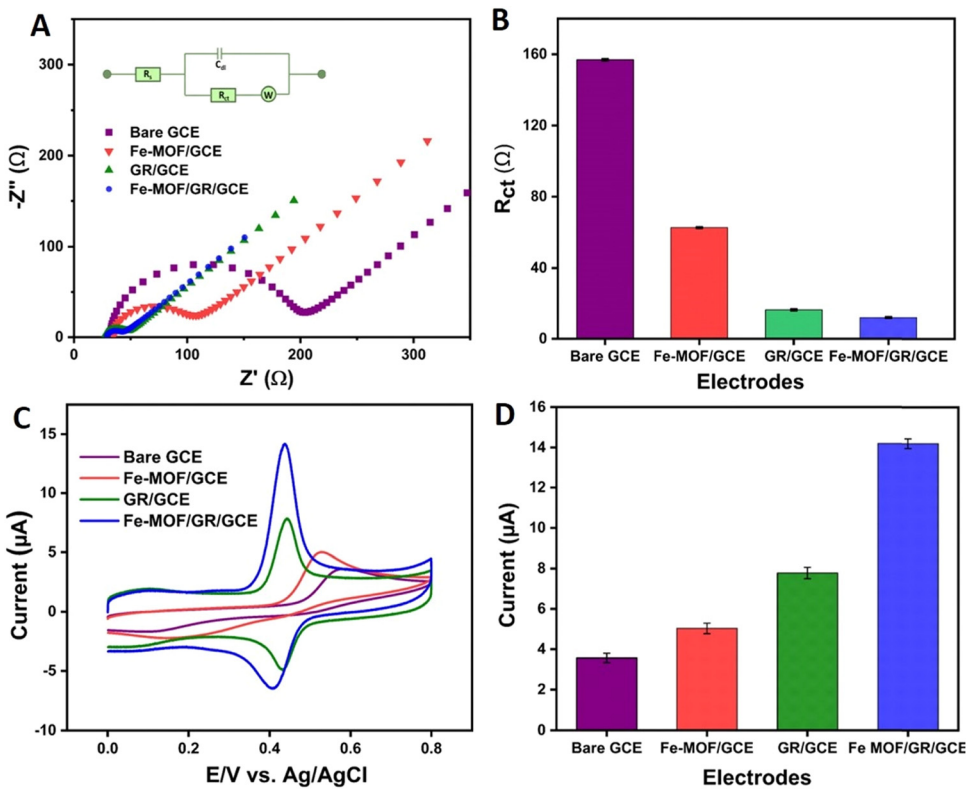

Fig. 4 (A) EIS plots of various electrodes in a solution of 5 mM $[Fe(CN)_6]^{3-/4-}$ and 0.1 M KCl (inset: Randles equivalent circuit model). (B) Corresponding bar diagram of R_{ct} values for various electrodes. (C) CV curves of various electrodes in the presence of 150 μM APAP at a scan rate of 50 mV s^{-1} in 0.05 M PBS at pH 7.0. (D) Comparison of peak oxidation current obtained for various electrodes.

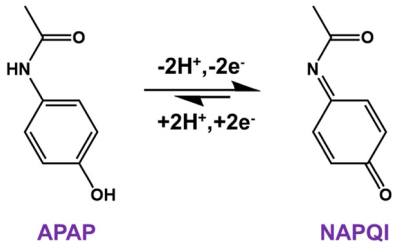

Scheme 1 Schematic diagram of the electrochemical reaction of APAP.

a quasi-reversible system. The redox reaction of APAP to form *N*-acetyl *p*-quinone imine (NAPQI) at the electrode can be explained by the previously proposed process involving a two-electron and two-proton transfer, as depicted in Scheme 1.[39] The enhanced activity is attributed to electrostatic and π–π interactions within the Fe-MOF/GR nanocomposite.[40] Besides, free amino groups in the Fe-MOF facilitate electron transfer for generating Fe^{2+} ions and promoting the Fenton-like activity.[37,41] The bar diagram in Fig. 4D presents the comparison of the peak oxidation current of APAP on different GCEs. The Fe-MOF/GR/GCE exhibits a 3.97-fold increase in the peak oxidation current compared to the bare GCE for APAP detection. Because of the largest peak oxidation current of the Fe-MOF/GR nanocomposite, it was chosen as the optimal electrode for further studies of APAP detection.

3.4 Optimization of the Fe-MOF/GR composite

The effect of the Fe-MOF/GR mixing ratio (1 : 1, 1 : 2, 1 : 3, 2 : 1, and 3 : 1) on the peak current for APAP detection was investigated. The analysis of CV curves for different ratios of Fe-MOF/GR nanocomposite in Fig. S11 shows that the peak oxidation current for the 1 : 1 ratio is the highest compared to those for other ratios. Both Fe-MOF and GR provide sufficient electroactive surface sites in the Fe-MOF/GR composite, where the Fe-MOF aids in adsorbing APAP molecules onto the surface, while the GR nanosheets facilitate electron diffusion on the electrode surface. Consequently, the Fe-MOF/GR nanocomposite with a 1 : 1 ratio can effectively generate the highest current response for APAP detection and is selected as the optimal electrocatalyst.

3.5 Influence of the pH value and scan rate

Considering the occurrence of proton transfer during the electrochemical detection of APAP, the effect of the electrolyte pH value on the sensing performance was investigated. The electrochemical response of APAP on the Fe-MOF/GR/GCE was evaluated using the CV method over the pH range from 3 to 11 with the CV curves shown in Fig. 5A. APAP exists in a hydrolyzed form at pH < 5 and in a hydroxylated form at pH > 9.[42] The comparison of the peak redox current in Fig. 5B shows that the optimized pH value is 7.0 because it exhibits a well-defined

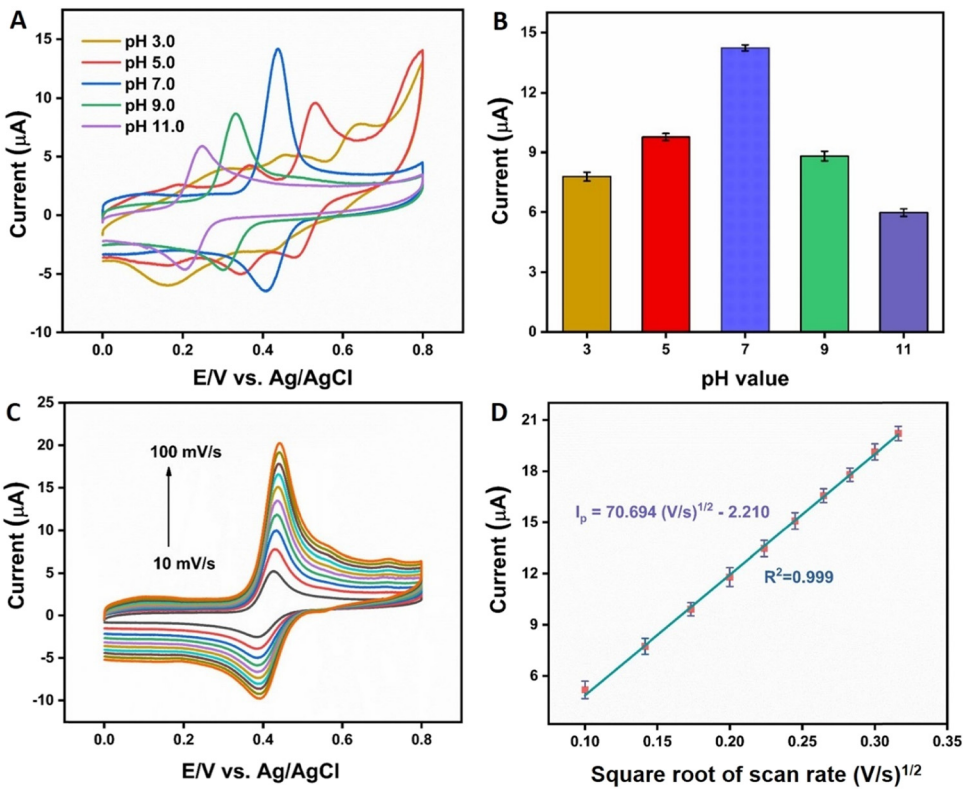

Fig. 5 (A) CV curves of the Fe-MOF/GR/GCE in 0.05 M PBS at different pH values. (B) Comparison of peak oxidation current obtained using the Fe-MOF/GR/GCE at various pH values. (C) CV curves of the Fe-MOF/GR/GCE in 0.05 M PBS containing 150 μM APAP at different scan rates. (D) Relationship between the peak oxidation current and the square root of the scan rate.

current peak with the highest peak oxidation current. According to the Nernst relation,[43] the linear analysis of the relationship between the peak oxidation potential and the pH value in Fig. S12 yields a slope of 0.051, which is close to the theoretical value of 0.059. Furthermore, based on Laviron's equation, the number of electrons involved in the electrochemical process was estimated to be approximately two, which was consistent with the reported redox mechanism. Therefore, the pH value of 7.0 was adopted for the subsequent electrochemical determination of APAP.

The influence of the scan rate on the electrochemical performance was investigated using the CV method in the presence of 150 μM APAP with the results shown in Fig. 5C. The peak redox current is observed to gradually increase with the scan rate ranging from 10 to 100 mV s^{-1}, indicating that the diffusion rate exceeds the reaction rate. The plot for the relation between the peak current and the square root of scan rate in Fig. 5D was analyzed and shows a correlation coefficient of 0.999. These results suggest that the electrochemical process on the Fe-MOF/GR/GCE is governed by diffusion-controlled mass transfer.[44]

3.6 Analytical performance of the Fe-MOF/GR/GCE

Fig. 6A shows the DPV curves of different concentrations of APAP in 0.05 M PBS at pH 7.0 on the Fe-MOF/GR/GCE. The peak oxidation current gradually increases with the APAP concentrations ranging from 0.05 to 175.3 μM. The linear relationship between the peak oxidation current and the APAP concentration in the range from 0.05 to 105.6 μM is observed in Fig. 6B with a correlation coefficient of 0.998. The LOD and the sensitivity were estimated using the following equations:

$$\mathrm{LOD} = 3\sigma/S$$

sensitivity = slope of the calibration curve/active surface area.

The LOD and the sensitivity for APAP detection were calculated to be 0.01 μM and 6.7 μA μM^{-1} cm^{-2}. The performance comparison of the Fe-MOF/GR nanocomposite with the previously reported electrocatalysts for APAP detection is displayed in Table 1. This comparison encompasses key analytical parameters, including the linear detection range, the LOD, and the sensitivity. The electrochemical sensor with the Fe-MOF/GR demonstrates a broad linear range (0.05–105.6 μM), a low LOD (0.010 μM), and a significantly higher sensitivity (6.7 μA μM^{-1} cm^{-2}) compared to most reported electrocatalysts.[18,45–52] In particular, the sensitivity of the proposed electrochemical sensor is markedly enhanced relative to the previously reported MOF- and carbon-based composites, while maintaining a competitive LOD and a wider dynamic range. These performance improvements can be attributed to the synergistic interaction between Fe-MOF and GR by enhancing electron transfer and increasing the availability of active sites. Overall, this comparative analysis highlights the superior analytical performance of the electrochemical sensor with the Fe-MOF/GR, underscoring its

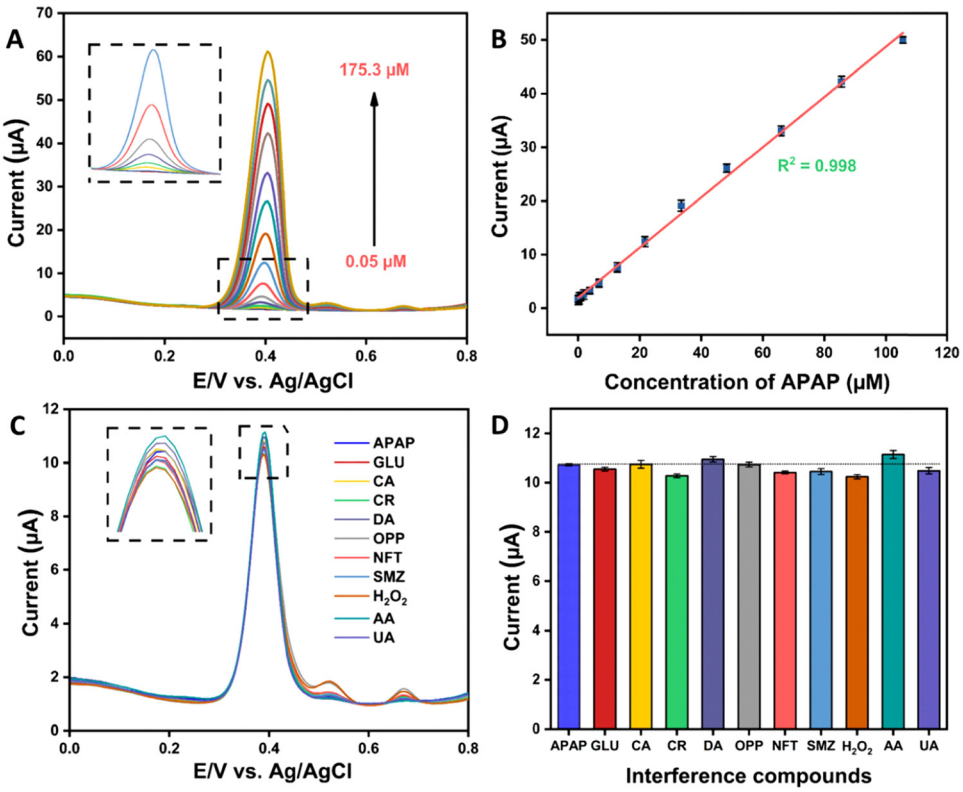

Fig. 6 (A) DPV curves of different concentrations of APAP on the Fe-MOF/GR/GCE. (B) Dependence of the peak oxidation current on the APAP concentration. (C) DPV curves of 20 μM APAP with different potential interference compounds on the Fe-MOF/GR/GCE. (D) Corresponding bar diagram of peak oxidation current for difference interference compounds.

Table 1 Performance comparison of various electrocatalysts for APAP detection

Electrocatalyst	Method	Linear range (μM)	LOD (μM)	Sensitivity (μA μM^{-1} cm^{-2})	Ref.
PEDOT/GO	CV	10–60	0.57	–	18
GO	DPV	0.165–26.5	0.04	–	45
CSS	DPV	0.37–7.52	0.12	0.02	46
NiO-CuO/GR	SWV	4–400	1.33	0.618	47
Lt/f-MWCNT	DPV	0.9–80.0	0.78	0.061	48
Cu-MOF@S-Gr	DPV	2–188	0.012	0.85	49
NiCo-MOF	CV	5–400	1.0	–	50
Sa-HDTMA/UiO-66	LSV	1–700	0.19	–	51
Co_3O_4@NHCS	DPV	1–200 000–8000	0.07	0.131	52
Fe-MOF/GR	DPV	0.05–105.6	0.010	6.7	This work

PEDOT – poly(3,4-ethylenedioxythiophene); GO – graphene oxide; CSS – carbon spherical shells; NiO – nickel oxide; CuO – copper oxide; SWV – square wave voltammetry; Lt – luteolin; f-MWCNT – functionalized multi-wall carbon nanotube; S-Gr – sulphur doped graphene; CC – carbon cloth; Sa-HDTMA – surfactant hexadecyl trimethyl ammonium; UiO-66 – University of Oslo-66 (zirconium 1,4-dicarboxybenzene MOF; LSV – linear sweep voltammetry; Co_3O_4 – cobalt oxide; NHCS – nitrogen-doped hollow carbon spheres.

potential as an efficient and reliable platform for APAP detection in practical applications.

3.7 Selectivity, repeatability, and reproducibility

To assess the selectivity of the Fe-MOF/GR/GCE, the impact of potential interference compounds on the peak current was studied using the DPV measurements performed at the fixed APAP concentration of 20 μM while introducing a 10-fold excess of interference compounds, including glucose (GLU), catechol (CA), creatinine (CR), dopamine (DA), o-phenyl phenol (OPP), nitrofurantoin (NFT), sulfamethazine (SMZ), hydrogen peroxide (H_2O_2), ascorbic acid (AA), and uric acid (UA). The DPV curves in Fig. 6C show that the presence of these interference compounds does not affect the shapes of the DPV curves for APAP detection. The corresponding distribution of peak oxidation current in Fig. 6D indicates that the variation of peak oxidation current is less than 7%. Therefore, the proposed electrochemical sensor for APAP detection exhibits excellent anti-interference capabilities and can be used to reliably detect APAP quantitatively.

To assess the repeatability of the Fe-MOF/GR/GCE, the CV curves for five successive determinations of 150 μM APAP were recorded and shown in Fig. 7A. The distribution of peak oxidation current in Fig. 7B demonstrates the relative standard deviation (RSD) of 1.6%, which indicates good repeatability. The reproducibility of the Fe-MOF/GR/GCE was evaluated by using five GCEs modified under identical conditions by the CV method with 150 μM APAP. Fig. 7C shows the corresponding CV curves in the reproducibility study. From Fig. 7D, the RSD of the peak oxidation current was calculated with the value of 2.02%. These findings confirm that the Fe-MOF/GR modified GCE exhibits satisfactory selectivity, repeatability, and reproducibility.

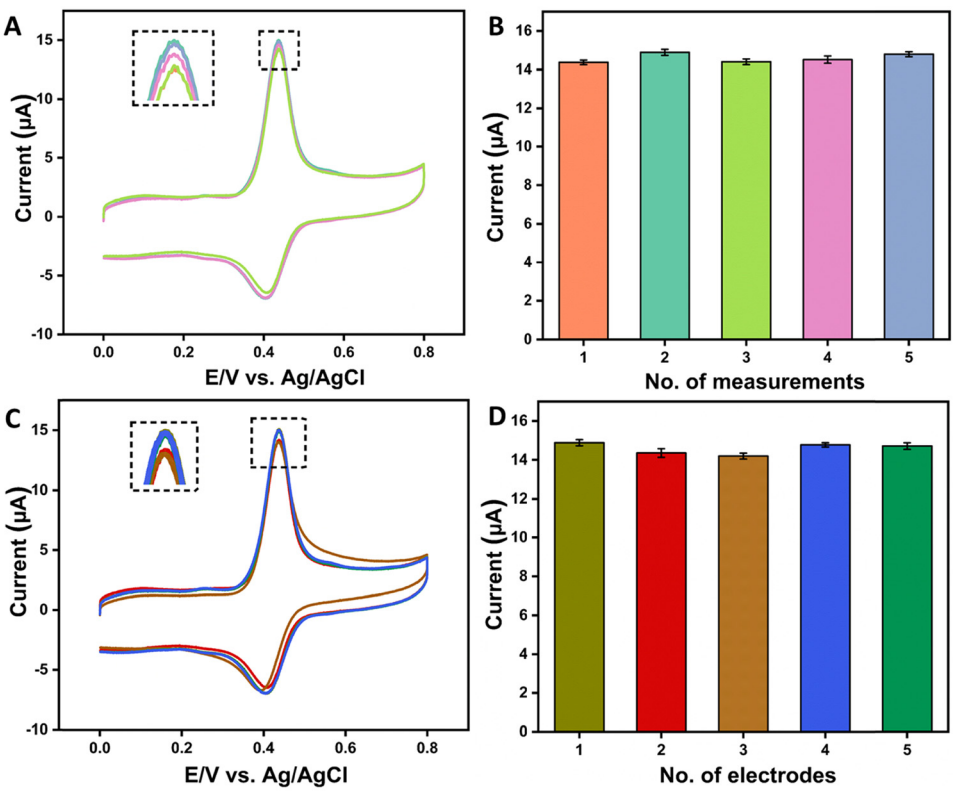

Fig. 7 (A) Repeatability study of the Fe-MOF/GR/GCE for the detection of 150 μM APAP. (B) Corresponding bar diagram of peak oxidation current. (C) Reproducibility study of the Fe-MOF/GR/GCE for the detection of 150 μM APAP. (D) Corresponding bar diagram of peak oxidation current.

3.8. Recovery experiments

Real-sample analysis is essential to evaluate the practical applicability of the developed sensor for detecting the target analyte in complex matrices. The performance of the Fe-MOF/GR/GCE was assessed by detecting APAP spiked in river water and artificial urine using the DPV method. River water was collected from the Xindian River in Taipei, followed by filtration and centrifugation to remove suspended particles. Artificial urine was prepared according to the standard protocol reported in the literature.[53] For validation, the standard HPLC analysis was carried out on the same samples under the optimized instrumental conditions, as detailed in the Instrumentation section of the SI. For river water samples, the HPLC method yielded the recovery values of 96.5–99.0%, while the electrochemical sensor with the Fe-MOF/GR/GCE exhibited the recovery values of 95.5–98.2%. For artificial urine samples, the HPLC method showed the recovery values of 96.0–97.5%, whereas the electrochemical sensor achieved the recovery values of 96.0–96.5%. The detailed results are summarized in Table S1. The close agreement between the results obtained from the HPLC method and the electrochemical sensor with the Fe-MOF/GR/GCE demonstrates the high accuracy and reliability of the developed electrochemical sensor. These results confirm its practical applicability for monitoring APAP in the environmental and biological samples.

4. Conclusions

In summary, we successfully developed a robust and reliable electrocatalyst by integrating Fe-MOF on GR nanosheets for sensitive electrochemical detection of APAP. The structural and morphological characterization of the Fe-MOF/GR nanocomposite was conducted using various techniques, including XRD, FTIR spectra, Raman spectra, XPS, FESEM, TEM, EDX, elemental mapping, and BET analysis. The exceptional performance of the Fe-MOF/GR-based electrochemical sensor can be attributed to the synergistic interaction between the Fe-MOF and the GR matrix by the engineered hybrid heterostructure. This nanocomposite design provides numerous active sites and efficient pathways for electron transport to significantly reduce the R_{ct} and enhance the ESCA. Besides, the conductive GR matrix plays a crucial role in improving the electrode's overall effectiveness during the electrochemical reaction. The Fe-MOF/GR based electrochemical sensor demonstrates impressive analytical performance for APAP detection, achieving a LOD of 10 nM, excellent sensitivity of 6.7 μA μM^{-1} cm^{-2}, a wide linear range of 0.05–105.6 μM, and remarkable selectivity of $<7\%$. Our findings highlight the practical applicability of this innovative electrocatalyst in real-world scenarios by the electrochemical detection of APAP in river water and artificial urine. This research not only advances the development of effective monitoring tools but also paves the way for innovative solutions in analytical chemistry.

Conflicts of interest

There are no conflicts to declare.

Data availability

The raw data required to reproduce these findings cannot be shared at this time as the data also form part of an ongoing study. Data will be released upon completion of the research project.

The supplementary information (SI) contains details on materials and instrumentation, Raman and XPS spectra, Zeta potential values, TEM and HRTEM images, EDX mapping, N_2 adsorption–desorption isotherms, CV characterization at various scan rates, optimization studies (pH and composite ratios), and a comparison table for real sample analysis. See DOI: https://doi.org/10.1039/d5tb02893k.

Acknowledgements

The authors gratefully acknowledge the support of the Ministry of Science and Technology of Taiwan for this research under grant MOST 111–2221-E-027–020-MY3, NSTC 114–2221-E-027–023-MY2, and NSTC 114–2221-E-027–120. The authors would also like to acknowledge the support from the Ministry of Human Resource Development (MHRD) of India under the Scheme for Promotion of Academic and Research Collaboration (SPARC) [No. SPARC/2019-2020/P2197/SL].

References

1 O. I. González Peña, M. Á. López Zavala and H. Cabral Ruelas, Pharmaceuticals market, consumption trends and disease incidence are not driving the pharmaceutical research on water and wastewater, *Int. J. Environ. Res. Public Health*, 2021, **18**, 2532.
2 W. J. Lee, P. S. Goh, W. J. Lau and A. F. Ismail, Removal of pharmaceutical contaminants from aqueous medium: a state-of-the-art review based on paracetamol, *Arab. J. Sci. Eng.*, 2020, **45**, 7109–7135.
3 W. M. Lee, Acetaminophen toxicity: a history of serendipity and unintended consequences, *Clin. Liver Dis.*, 2020, **16**, 34–44.
4 A. Ramachandran and H. Jaeschke, Acetaminophen toxicity: novel insights into mechanisms and future perspectives, *Gene Expression*, 2018, **18**, 19.
5 A. Marın, E. Garcıa, A. Garcıa and C. Barbas, Validation of a HPLC quantification of acetaminophen, phenylephrine and chlorpheniramine in pharmaceutical formulations: capsules and sachets, *J. Pharm. Biomed. Anal.*, 2002, **29**, 701–714.
6 C. Celma, J. A. Allue, J. Prunonosa, C. Peraire and R. Obach, Simultaneous determination of paracetamol and chlorpheniramine in human plasma by liquid chromatography–tandem mass spectrometry, *J. Chromatogr. A*, 2000, **870**, 77–86.

7 F. Shihana, D. Dissanayake, P. Dargan and A. Dawson, A modified low-cost colorimetric method for paracetamol (acetaminophen) measurement in plasma, *Clin. Toxicol.*, 2010, **48**, 42–46.
8 X. Liu, W. Na, H. Liu and X. Su, Fluorescence turn-off-on probe based on polypyrrole/graphene quantum composites for selective and sensitive detection of paracetamol and ascorbic acid, *Biosens. Bioelectron.*, 2017, **98**, 222–226.
9 W. Ruengsitagoon, S. Liawruangrath and A. Townshend, Flow injection chemiluminescence determination of paracetamol, *Talanta*, 2006, **69**, 976–983.
10 Q. Chu, L. Jiang, X. Tian and J. Ye, Rapid determination of acetaminophen and p-aminophenol in pharmaceutical formulations using miniaturized capillary electrophoresis with amperometric detection, *Anal. Chim. Acta*, 2008, **606**, 246–251.
11 S. Ganesan, T. Kokulnathan and A. Palaniappan, Investigating the electrochemical detection of chlorpromazine and cytocompatibility of 2D/2D molybdenum diselenide/vanadium carbide-based nanocomposites, *J. Environ. Chem. Eng.*, 2025, **13**(6), 19404.
12 B. Kulkarni, T. Kokulnathan, T. J. Wang, M. M. Al-Ansari and R. G. Balakrishna, Trace-level electrochemical detection of organic pollutant metol in environmental samples using MIL-101 (Cr)@ F-MWCNTs nanocomposite, *J. Environ. Chem. Eng.*, 2025, **13**(6), 119262.
13 T. Kokulnathan, S. Ganesan, T.-J. Wang and A. Palaniappan, Mechanochemically synthesized flower-like bismuth oxyhalides: An electrochemical platform for diclofenac detection, *J. Environ. Chem. Eng*, 2024, **12**, 114049.
14 R. Vishnuraj, T. Kokulnathan, T.-J. Wang, M. Rangarajan and B. Pullithadathil, Enhanced electrochemical detection of cardioselective beta-blocker acebutolol using coaxially electrospun gold nanograins decorated tin oxide nanofibers, *J. Alloys Compd.*, 2025, **1014**, 178600.
15 A. U. Alam, Y. Qin, M. M. R. Howlader, N.-X. Hu and M. J. Deen, Electrochemical sensing of acetaminophen using multi-walled carbon nanotube and β-cyclodextrin, *Sens. Actuators, B*, 2018, **254**, 896–909.
16 B.-R. Adhikari, M. Govindhan and A. Chen, Sensitive detection of acetaminophen with graphene-based electrochemical sensor, *Electrochim. Acta*, 2015, **162**, 198–204.
17 L. Jiang, S. Gu, Y. Ding, F. Jiang and Z. Zhang, Facile and novel electrochemical preparation of a graphene–transition metal oxide nanocomposite for ultrasensitive electrochemical sensing of acetaminophen and phenacetin, *Nanoscale*, 2014, **6**, 207–214.
18 W. Si, W. Lei, Z. Han, Y. Zhang, Q. Hao and M. Xia, Electrochemical sensing of acetaminophen based on poly (3, 4-ethylenedioxythiophene)/graphene oxide composites, *Sens. Actuators, B*, 2014, **193**, 823–829.
19 T. Jia, Y. Gu and F. Li, Progress and potential of metal-organic frameworks (MOFs) for gas storage and separation: A review, *J. Environ. Chem. Eng.*, 2022, **10**, 108300.
20 C. Yazhini, M. Rajamani, J. Rafi, E. Es, R. Thapa and B. Neppolian, From MOF to terbium-doped MOF: Investigating the role of bimetals in hybrid environment towards the sensing mechanism of antibiotic in water, *Appl. Mater. Today*, 2025, **43**, 102643.
21 R. Du, Y. Wu, Y. Yang, T. Zhai, T. Zhou, Q. Shang, L. Zhu, C. Shang and Z. Guo, Porosity engineering of MOF-based materials for electrochemical energy storage, *Adv. Energy Mater.*, 2021, **11**, 2100154.
22 J. S. Jeyaprakash, M. Rajamani, C. L. Bianchi, M. Ashokkumar and B. Neppolian, Highly efficient ultrasound-driven Cu-MOF/$ZnWO_4$ heterostructure: An efficient visible-light photocatalyst with robust stability for complete degradation of tetracycline, *Ultrason. Sonochem.*, 2023, **100**, 106624.
23 I. Salahshoori, M. N. Jorabchi, S. Ghasemi, M. Golriz, S. Wohlrab and H. A. Khonakdar, An in silico study of sustainable drug pollutants removal using carboxylic acid functionalized-MOF nanostructures (MIL-53 (Al)-$(COOH)_2$): Towards a greener future, *Desalination*, 2023, **559**, 116654.
24 A. A. Mouhamed, A. H. Nadim, A. M. Mahmoud, N. M. Mostafa and B. M. Eltanany, Bimetallic MOF-based electrochemical sensor for determination of paracetamol in spiked human plasma, *BMC Chem.*, 2024, **18**, 148.
25 Y. L. Wang, S. Zhang, Y. F. Zhao, J. Bedia, J. J. Rodriguez and C. Belver, UiO-66-based metal organic frameworks for the photodegradation of acetaminophen under simulated solar irradiation, *J. Environ. Chem. Eng.*, 2021, **9**, 106087.
26 X.-X. Zheng, L.-J. Shen, X.-P. Chen, X.-H. Zheng, C.-T. Au and L.-L. Jiang, Amino-modified Fe-terephthalate metal–organic framework as an efficient catalyst for the selective oxidation of H_2S, *Inorg. Chem.*, 2018, **57**, 10081–10089.
27 A. D. S. Barbosa, D. Julião, D. M. Fernandes, A. F. Peixoto, C. Freire, B. de Castro, C. M. Granadeiro, S. S. Balula and L. Cunha-Silva, Catalytic performance and electrochemical behaviour of Metal–organic frameworks: MIL-101 (Fe) versus NH_2-MIL-101 (Fe), *Polyhedron*, 2017, **127**, 464–470.
28 Y. Dong, T. Hu, M. Pudukudy, H. Su, L. Jiang, S. Shan and Q. Jia, Influence of microwave-assisted synthesis on the structural and textural properties of mesoporous MIL-101 (Fe) and NH_2-MIL-101 (Fe) for enhanced tetracycline adsorption, *Mater. Chem. Phys.*, 2020, **251**, 123060.
29 A. A. Taha, L. Huang, S. Ramakrishna and Y. Liu, MOF [NH_2-MIL-101 (Fe)] as a powerful and reusable Fenton-like catalyst, *J. Water Process Eng.*, 2020, **33**, 101004.
30 M. Daniel, G. Mathew, M. Anpo and B. Neppolian, MOF based electrochemical sensors for the detection of physiologically relevant biomolecules: An overview, *Coord. Chem. Rev.*, 2022, **468**, 214627.
31 Y. Zheng, S. Zheng, H. Xue and H. Pang, Metal-organic frameworks/graphene-based materials: preparations and applications, *Adv. Funct. Mater.*, 2018, **28**, 1804950.
32 Z. Zhang, X. Li, B. Liu, Q. Zhao and G. Chen, Hexagonal microspindle of NH_2-MIL-101 (Fe) metal–organic frameworks with visible-light-induced photocatalytic activity for the degradation of toluene, *RSC Adv.*, 2016, **6**, 4289–4295.
33 S.-W. Lv, J.-M. Liu, C.-Y. Li, N. Zhao, Z.-H. Wang and S. Wang, A novel and universal metal-organic frameworks

sensing platform for selective detection and efficient removal of heavy metal ions, *Chem. Eng. J.*, 2019, **375**, 122111.
34 T. Kokulnathan and S.-M. Chen, Robust and selective electrochemical detection of antibiotic residues: The case of integrated lutetium vanadate/graphene sheets architectures, *J. Hazard. Mater.*, 2020, **384**, 121304.
35 K. Vinothkumar and R. G. Balakrishna, One-pot synthesis of NH_2-MIL-101 (Fe) and α–Fe_2O_3 composite as efficient heterojunction for multifunctional photocatalytic membranes: Towards zero waste generation, *Appl. Catal., B*, 2024, **340**, 123199.
36 A. C. Ferrari and D. M. Basko, Raman spectroscopy as a versatile tool for studying the properties of graphene, *Nat. Nanotechnol.*, 2013, **8**, 235–246.
37 P. Huang, L. Yao, Q. Chang, Y. Sha, G. Jiang, S. Zhang and Z. Li, Room-temperature preparation of highly efficient NH_2-MIL-101 (Fe) catalyst: The important role of–NH_2 in accelerating Fe (III)/Fe (II) cycling, *Chemosphere*, 2022, **291**, 133026.
38 J. Rafi, A. Rajan and B. Neppolian, Enhanced electrocatalytic performance of aluminium metal-organic framework towards the detection of broad-spectrum chloramphenicol antibiotic, *Electrochim. Acta*, 2023, **446**, 142079.
39 D. Nematollahi, H. Shayani-Jam, M. Alimoradi and S. Niroomand, Electrochemical oxidation of acetaminophen in aqueous solutions: Kinetic evaluation of hydrolysis, hydroxylation and dimerization processes, *Electrochim. Acta*, 2009, **54**, 7407–7415.
40 E. Chiavazza, S. Berto, A. Giacomino, M. Malandrino, C. Barolo, E. Prenesti, D. Vione and O. Abollino, Electrocatalysis in the oxidation of acetaminophen with an electrochemically activated glassy carbon electrode, *Electrochim. Acta*, 2016, **192**, 139–147.
41 D. Pattappan, K. V. Kavya, S. Vargheese, R. T. R. Kumar and Y. Haldorai, Graphitic carbon nitride/NH_2-MIL-101 (Fe) composite for environmental remediation: Visible-light-assisted photocatalytic degradation of acetaminophen and reduction of hexavalent chromium, *Chemosphere*, 2022, **286**, 131875.
42 D. J. Miner, J. R. Rice, R. M. Riggin and P. T. Kissinger, Voltammetry of acetaminophen and its metabolites, *Anal. Chem.*, 1981, **53**, 2258–2263.
43 M. M. Walczak, D. A. Dryer, D. D. Jacobson, M. G. Foss and N. T. Flynn, pH dependent redox couple: An illustration of the Nernst equation, *J. Chem. Educ.*, 1997, **74**, 1195.
44 J. Rafi, M. Daniel and B. Neppolian, Ultrasensitive detection of chloramphenicol in water using functionalized polymers with an Aluminium organic framework, *Chemosphere*, 2024, 141981.
45 J. Song, J. Yang, J. Zeng, J. Tan and L. Zhang, Graphite oxide film-modified electrode as an electrochemical sensor for acetaminophen, *Appl. Catal., B*, 2011, **155**, 220–225.
46 A. M. Campos, P. A. Raymundo-Pereira, C. D. Mendonca, M. L. Calegaro, S. A. S. Machado and O. N. Oliveira Jr, Size control of carbon spherical shells for sensitive detection of paracetamol in sweat, saliva, and urine, *ACS Appl. Nano Mater.*, 2018, **1**, 654–661.
47 B. Liu, X. Ouyang, Y. Ding, L. Luo, D. Xu and Y. Ning, Electrochemical preparation of nickel and copper oxides-decorated graphene composite for simultaneous determination of dopamine, acetaminophen and tryptophan, *Talanta*, 2016, **146**, 114–121.
48 M. Amiri-Aref, J. B. Raoof and R. Ojani, A highly sensitive electrochemical sensor for simultaneous voltammetric determination of noradrenaline, acetaminophen, xanthine and caffeine based on a flavonoid nanostructured modified glassy carbon electrode, *Appl. Catal., B*, 2014, **192**, 634–641.
49 S. Nabi, F. A. Sofi, N. Rashid, P. P. Ingole and M. A. Bhat, Metal–organic framework functionalized sulphur doped graphene: a promising platform for selective and sensitive electrochemical sensing of acetaminophen, dopamine and H_2O_2, *New J. Chem.*, 2022, **46**, 1588–1600.
50 X.-L. Liu, J.-W. Guo, Y.-W. Wang, A.-Z. Wang, X. Yu and L.-H. Ding, A flexible electrochemical sensor for paracetamol based on porous honeycomb-like NiCo-MOF nanosheets, *Rare Met.*, 2023, **42**, 3311–3317.
51 M. C. N. Ngwem, J. C. Kemmegne-Mbouguen, H. W. Langmi, N. M. Musyoka and R. Mokaya, Electrochemical sensor for ascorbic acid, acetaminophen and nitrite based on organoclay/Zr-MOF film modified glassy carbon electrode, *ChemistrySelect*, 2022, **7**, e202202308.
52 V. Duraisamy, V. Sudha, V. Dharuman and S. M. Senthil Kumar, Highly efficient electrochemical sensing of acetaminophen by cobalt oxide-embedded nitrogen-doped hollow carbon spheres, *ACS Biomater. Sci. Eng.*, 2023, **9**, 1682–1693.
53 B. Shmaefsky, Artificial urine for laboratory testing: revisited, *Am. Biol. Teach.*, 1995, **57**, 428–430.